In Situ Reproducible Sharp Tips for Atomic Force Microscopy

Jo Onoda,[1,*] Tsuyoshi Hasegawa,[2] and Yoshiaki Sugimoto[3]

[1] *Department of Physics, University of Alberta, Edmonton, Alberta T6G 2J1, Canada*
[2] *Department of Applied Physics, Waseda University, 3-4-1 Okubo, Shinjuku-ku, Tokyo, 169-8555, Japan*
[3] *Department of Advanced Materials Science, University of Tokyo, 5-1-5 Kashiwanoha, Kashiwa, Chiba, 277-8561, Japan*

(Received 29 December 2020; revised 2 February 2021; accepted 2 March 2021; published 26 March 2021)

Atomically sharp tips are a requirement for scanning-probe microscopy, such as scanning tunneling microscopy (STM) and atomic force microscopy (AFM). Compared with STM, AFM imaging is more sensitive to the sharpness of tip apices because long-range forces act as a background signal on the high-resolution AFM images originating from short-range forces. Here we report the investigation of *in situ* reproducible sharp tips for AFM. We make an Ag_2S crystal, a mixed ionic and electronic conductor, on a conventional Si cantilever, and controllably grow and shrink the Ag nanoprotrusion by changing the polarity of the bias voltage between the tip and the sample. We are able to reduce the contribution of long-range forces by growing a Ag nanoprotrusion on the Ag_2S tip, and obtain atomic-resolution AFM images. We also confirm that the Ag_2S tip with a Ag nanoprotrusion, the end of which presumably terminates in Si atoms, is capable of simultaneous AFM and STM measurements.

DOI: 10.1103/PhysRevApplied.15.034079

I. INTRODUCTION

Atomic force microscopy (AFM) is widely used to image sample surfaces at atomic resolution and to measure the interaction force between the tip and the sample. The measured force is composed of long-range and short-range forces. While the former originate from electrostatic and van der Waals forces and act as a background signal, the latter are the origin of atomic-resolution AFM images, which are exemplified by chemical attractive [1] and Pauli repulsive [2] forces. Lantz *et al.* [3] proposed the well-known "on-minus-off" method for separating long-range and short-range forces, which uses the surface sites where the short-range force does not exist; for example, corner holes of the Si(111)-(7 × 7) surface. In this way, extraction of the short-range chemical force (or energy) becomes possible, enabling us to not only discriminate the chemical identities of individual surface [4] and tip [5] atoms but also to evaluate electronegativity at the atomic scale [6].

While this force-separation method has been developed for the postprocessing stage, tremendous effort has also been made to exclusively measure the short-range component in experiments. Since AFM operation with a small oscillation amplitude can increase the component of short-range forces [7], the use of AFM probes with high stiffness, such as qPlus [8] and Koribli [9] sensors, is becoming mainstream in the field of atomic-resolution AFM at low temperature.

Nevertheless, the long-range component remains the signal that needs to be reduced substantially. In frequency-modulated AFM, the frequency shift (Δf) from the resonance frequency (f_0) is the detection signal of interest. Since the mechanical noise in Δf is proportional to the gradient of Δf [10], the signal-to-noise ratio unavoidably decreases. To reduce the long-range forces, we need to use high-aspect-ratio materials such as carbon nanotubes [11–13] or metal tips sharpened by means of a focused ion beam [14,15] and/or field-ion microscopy [16–19]. However, tips usually have to be transferred to *ex situ* preparation apparatuses whenever sharp tip apices are needed. On the other hand, tip sharpening by single-atom or single-molecule functionalization has been one of the most successful *in situ* methods in the last decade for AFM [20,21], although a low temperature (4.5 K) is necessary to stabilize the atom or molecule attachment.

Here we report *in situ* reproducible sharp tips for AFM that can be implemented even at room temperature. Ag_2S crystals, which are a mixed ionic and electronic conductor, have been investigated as practical-use atomic switches [22–24]. The growth and shrinkage of a Ag nanoprotrusion at the apex of Ag_2S tips can be reversibly controlled by the polarity of the applied bias voltage between the tip and the sample under the operation of scanning tunneling microscopy (STM) [24]. Since the scanning electron micrograph of Terabe *et al.* [22] shows that the Ag

*jonoda@ualberta.ca

nanoprotrusion has a filamentary shape, its growth would drive the large tip body back from the surface and give a smaller, effectively "sharp" tip radius. We confirm that such a Ag_2S crystal can be fabricated on a conventional Si cantilever. We are able to reduce the contribution of the long-range forces by fabricating a Ag nanoprotrusion on the Ag_2S tip, whose radius of curvature is evaluated by force spectroscopy. Owing to the growth of the Ag nanoprotrusion, the end of which presumably terminates in Si atoms, we obtain atomically resolved AFM images even with a blunt Ag_2S tip. It is also found that simultaneous AFM and STM measurements are possible. These results are highly positive, suggesting that once we cover a conventional AFM tip (such as made of Si or W) with a Ag_2S crystal, we will be able to sharpen the tip apex *in situ* and reduce the effect of the long-range force in every subsequent AFM experiment.

II. METHODS AND PRINCIPLES

All experiments are performed with a custom-built frequency-modulation atomic force microscope at room temperature in an ultrahigh-vacuum chamber (the base pressure is typically less than 1×10^{-8} Pa). An optical interferometer is used to detect the cantilever deflection, and a frequency-modulation technique is used to obtain Δf from f_0. The cantilever-oscillation amplitude is set to be sufficiently large (100–150 Å) for stable AFM operation. To compensate for the contact potential difference between the tip and the sample, a proper voltage is applied between them. Ag_2S tips are fabricated in a different chamber. We deposit Ag layers, nominally 20 nm thick, onto commercially available Si cantilevers and sulfurize them in a sulfur vapor at 100 °C [22]. The fabricated Ag_2S tips are then mounted in the AFM chamber. We use clean Ag(111) and Si(111)-(7 × 7) surfaces to study the growth and shrinkage of the Ag nanoprotrusion. The Ag(111) surface is cleaned by repeated Ar^+ sputtering (2 keV, 1×10^{-3} Pa for 20 min) and annealing at 600 °C in an ultrahigh vacuum. A clean Si(111)-(7 × 7) surface is prepared by repeated flashing of Si(111) samples to 1250 °C after degassing at 650 °C overnight. Force spectroscopy on a Si adatom is performed with atom-tracking and feedforward systems [25]. Additional details have been described elsewhere [6].

The principle of Ag-nanoprotrusion growth and shrinkage on a Ag_2S crystal is shown schematically in Fig. 1. When we apply a negative bias voltage to the sample and inject electrons into the Ag_2S crystal, Ag^+ cations are reduced ($Ag^+_{(Ag_2S)} + e^- \rightarrow Ag_{(cluster)}$) and Ag atoms start to precipitate onto the Ag_2S surface. Ag^+ cations are continuously supplied from the underlying Ag layer to the Ag_2S surface because of the positive electric field toward the sample. The concentration of Ag^+ cations increases the electrochemical potential of the Ag^+ cations, and then

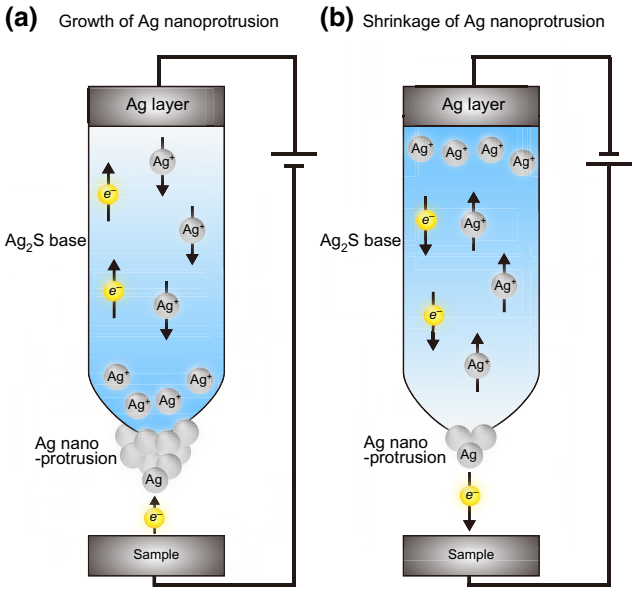

FIG. 1. Mechanisms of growth and shrinkage of the Ag nanoprotrusion. (a) When a negative bias voltage is applied to the sample, reduction of Ag^+ cations proceeds and Ag atoms are precipitated on the surface of the Ag_2S base. (b) When a positive bias voltage is applied to the sample, Ag^+ cations migrate toward the bottom of the Ag_2S base, which induces the oxidation of Ag atoms on the surface.

lowers the activation energy for reduction [24]. Thus, the reduction promotes the growth of the Ag cluster. On the other hand, when we apply a positive bias voltage to the sample, it induces the migration of Ag^+ cations toward the bottom of the Ag_2S crystal, causing a decrease of the Ag^+ concentration around the Ag_2S surface. As a result, the activation barrier for oxidation ($Ag_{(cluster)} \rightarrow Ag^+_{(Ag_2S)} + e^-$) becomes smaller and promotes the shrinkage of the Ag cluster. Thus, the growth and shrinkage of the Ag cluster is a reversible, iterative process. Such an Ag cluster can stably exist as long as no bias voltages larger than the threshold bias are applied. The Ag_2S atomic switch can be operated even at a frequency of 1 MHz with a sophisticated crossbar structure [23].

III. RESULTS AND DISCUSSION

Figure 2 shows how the height of the fabricated Ag_2S evolves with time on a Ag(111) surface. The tip height is estimated by the displacement of the piezoelctric material for the z direction in constant-current STM mode. The cantilever is not oscillated. When we apply a sample bias (V_S) of −4 V with a tunneling current (I_t) of 10 nA, the tip extends linearly over time as shown in Fig. 2(a). We then increase the tunneling current to 15 nA [at around 3000 s in Fig. 2(a)] and find the growth rate increases from 1.6 to 5.6 pm/s. It is known that the growth rate of a

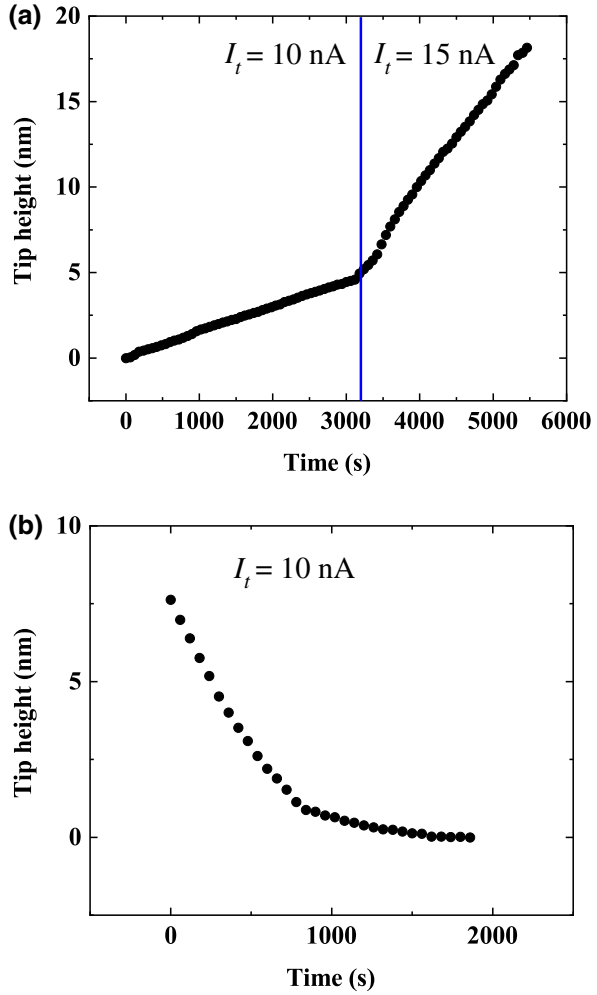

FIG. 2. Tip-height change during the growth and shrinkage of a Ag nanoprotrusion on the clean Ag(111) surface. (a) Growth mode with $I_t = 10$ nA and $V_S = -4$ V. The set point is changed to 15 nA at around 3000 s (blue line). (b) Shrinkage mode with $I_t = 10$ nA and $V_S = +4$ V. The experiments for (a),(b) are conducted in constant-current STM mode without cantilever oscillation.

Ag_2S tip shows an exponential dependence on the injected current [22,24]. Since the amount of injected current is constant, the fact that the growth rate is constant indicates that the Ag nanoprotrusion on the Ag_2S base grows with a filamentary shape as observed in the scanning electron micrograph in Ref. [22]. We also find that when we apply $V_S = +4$ V with $I_t = 10$ nA, the tip height decreases with time [Fig. 2(b)]. The change of the shrinkage rate at around 1000 s in Fig. 2(b) is presumably caused by either or both of the following factors. The first is the complete shrinkage of the cylindrical body of the Ag nanoprotrusion, which results in the change of the tip shape from filamentary to hemispherical. The other is that the cylindrical body still remains but the shrinkage of the Ag nanoprotrusion might have caused the concentration of Ag^+ cations immediately beneath the interface between the Ag nanoprotrusion and the Ag_2S base. This hinders the oxidation of Ag atoms, thus decreasing the dissolution rate of Ag atoms.

We investigate the reproducible growth and shrinkage of a Ag_2S tip with the interaction forces acquired on the Si(111)-(7 × 7) surface. We first confirm that the Ag_2S tip gives atomic-resolution images, and then we deliberately crash the tip into the surface. A $\Delta f\,(z)$ curve obtained with the crashed tip is shown as state 1 in Fig. 3. Since an abrupt change of Δf, which indicates the short-range chemical force, is not observed near the surface (around $z = 75$ Å), we find that the tip apex becomes blunt and shows only the long-range forces in the $\Delta f\,(z)$ curve. We then apply $V_S = -4$ V with $I_t = 10$ nA to fabricate a Ag nanoprotrusion on the Ag_2S base. Whenever we grow or shrink the nanoprotrusion, we temporarily stop the cantilever oscillation. As shown with state 2 in Fig. 3, the $\Delta f\,(z)$ curve obtained after the tip modification clearly shows a steep change from around 250 Å, indicating the emergence of the short-range force. The z position of the onset of the short-range force also indicates that the height of the grown Ag nanoprotrusion is at least 25 nm. We then apply $V_S = +4$ V with the same tunneling current, $I_t = 10$ nA, and obtain a $\Delta f\,(z)$ curve with the tip (state 3 in Fig. 3). The transition from state 2 to state 3 indicates the shrinkage of the Ag nanoprotrusion. We then repeat the growth of the nanoprotrusion with the same conditions ($V_S = -4$ V, $I_t = 10$ nA) as shown in state 4 in Fig. 3,

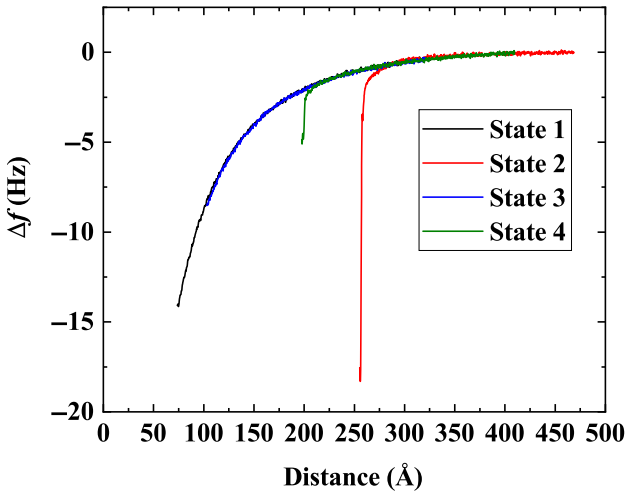

FIG. 3. $\Delta f\,(z)$ curves measured on the Si(111)-(7 × 7) surface with various states of a Ag_2S tip: state 1, after intentional crash of the tip into the surface; state 2, after the first growth of a Ag nanoprotrusion; state 3, after the shrinkage of the nanoprotrusion; state 4, after the second growth of the nanoprotrusion. The origin of the graph describes the divergence point of a fitted $\Delta f\,(z)$ curve for State 1 (not shown). The acquisition parameters are the resonance frequency $f_0 = 142.818$ kHz, the cantilever-oscillation amplitude $A = 145$ Å, the spring constant $k = 22.8$ N/m, and $V_S = -100$ mV.

and find that the height of the grown Ag nanoprotrusion is at least 20 nm the second time, shorter than the first time with state 2. The transitions of the states in Fig. 3 prove the reproducibility of the sharpness of the Ag_2S tip.

Figure 4(a) presents another set of $\Delta f\,(z)$ curves obtained with the Ag_2S tip with and without a Ag nanoprotrusion. These $\Delta f\,(z)$ curves are converted to force curves, $F(z)$, by the Sader method [26], as shown in Fig. 4(b).

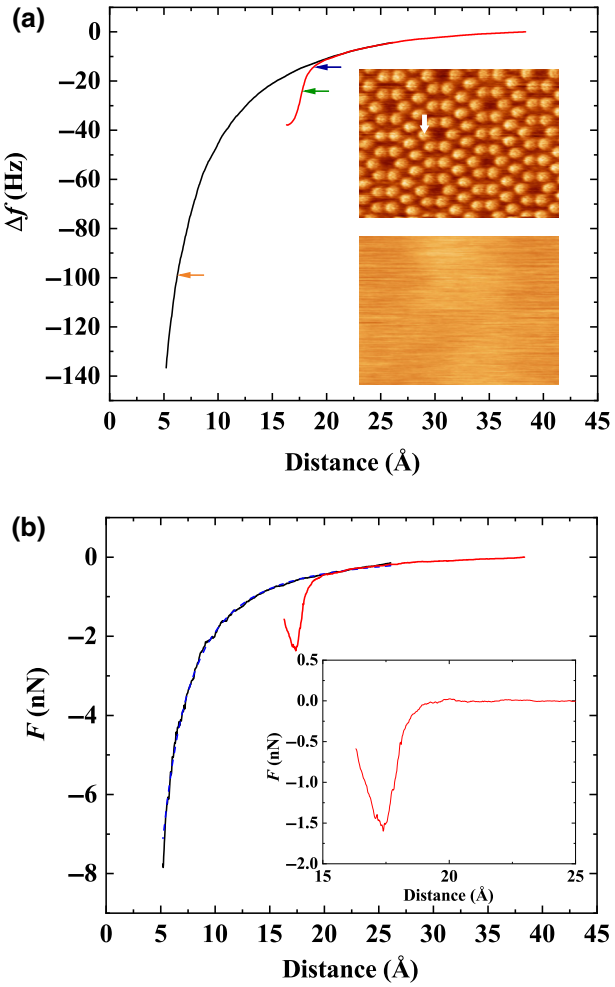

FIG. 4. Force-spectroscopy data for the Si(111)-(7 × 7) surface with a Ag_2S tip with and without a Ag nanoprotrusion. (a) $\Delta f\,(z)$ curves measured above the Si adatom (white arrow in the upper inset) with a Ag nanoprotrusion (red curve) and without the protrusion (black curve). The image in the upper inset is taken with the set point of $\Delta f = -24.4$ Hz, represented by the green arrow on the red curve, while the image in the lower inset is obtained with the set point of $\Delta f = -99.1$ Hz, indicated by the orange arrow on the black curve. (b) $F(z)$ curves converted from the $\Delta f\,(z)$ curves in (a). The long-range force (black curve) is fitted with $F_{\mathrm{vdW}}(z)$ (blue curve). The inset in (b) shows the short-range-force curve measured on the Si adatom. The origins of the graphs describe the divergence point of the long-range force. The acquisition parameters are $f_0 = 150.618$ kHz, $A = 173$ Å, $k = 26.7$ N/m, and $V_S = -200$ mV.

Since the $F(z)$ curve for no Ag nanoprotrusion includes only a long-range-force component, we fit it with the following equation for the van der Waals force, $F_{\mathrm{vdW}}(z)$:

$$F_{\mathrm{vdW}}(z) = -\frac{A_H R}{6z^2}, \tag{1}$$

where $A_H = 1.4 \times 10^{-19}$ J is the Hamaker constant for the mixed system of Ag_2S, a vacuum, and Si (see the Appendix for details on the estimation of the Hamaker constant) and R is the radius of curvature of the Ag_2S base. The fitted curve is shown in blue in Fig. 4(b), giving $R = 82$ nm. Compared with the radii of curvature of commercially available normal Si tips (a few nanometers) and metal-coated Si tips (10–30 nm), the value for the Ag_2S base is larger. The image in the lower inset in Fig. 4(a) is acquired with the Ag_2S tip without the Ag nanoprotrusion [the set point is indicated by the orange arrow on the black curve in Fig. 4(a)], showing the difficulty of obtaining atomic-resolution AFM images. On the other hand, we are able to observe individual Si adatoms with a Ag nanoprotrusion, as shown in the upper inset in Fig. 4(a) [the set point is indicated by the green arrow on the red curve in Fig. 4(a)]. Note that the red curve in Fig. 4(a) is measured at one of the Si atoms at the corner adatom sites in a faulted half-unit-cell [white arrow in the upper inset in Fig. 4(a)].

By subtracting the long-range-force component from the curve for the Ag_2S tip with the Ag nanoprotrusion, we obtain the short-range force exerted on the Si atom, as shown in the inset in Fig. 4(b). The maximum attractive force (F_{max}) is estimated to be 1.6 nN. According to Sugimoto *et al.* [27], that value is within the range of F_{max} for the junction between Si-tip and Si-surface atoms (0.5 nN $< F_{\mathrm{max}} <$ 2.5 nN). Even after we fabricate a Ag nanoprotrusion on the Ag_2S base, tip conditioning by mild contact with the Si surface (the typical tip insertion depth is 20–40 pm toward the surface from the height regulated by the Δf set point) is necessary. Thus, the very end of the tip apex presumably terminates in a Si cluster, giving rise to such F_{max} on the Si adatom.

We also investigate I_t simultaneously obtained with F. Since the bandwidth of a current-to-voltage converter (typically 1 kHz) is much smaller than f_0 (about 150 kHz for our Si cantilever), the time-averaged tunneling current ($\langle I_t \rangle$) is the signal observed in experiments. Figure 5(a) shows $\Delta f\,(z)$ and $\langle I_t(z) \rangle$ curves simultaneously measured on the Si adatom in the upper inset in Fig. 4(a). Using the conversion method for the tunneling current [28], we deduce the $I_t(z)$, which is the quantity comparable to I_t in conventional static STM. The converted $F(z)$ and $I_t(z)$ curves are shown in Fig. 5(b). In the close-distance range, where F reaches F_{max}, we find a strong reduction of I_t. This phenomenon is related to a modification of the electronic structure of the surface adatom due to the formation

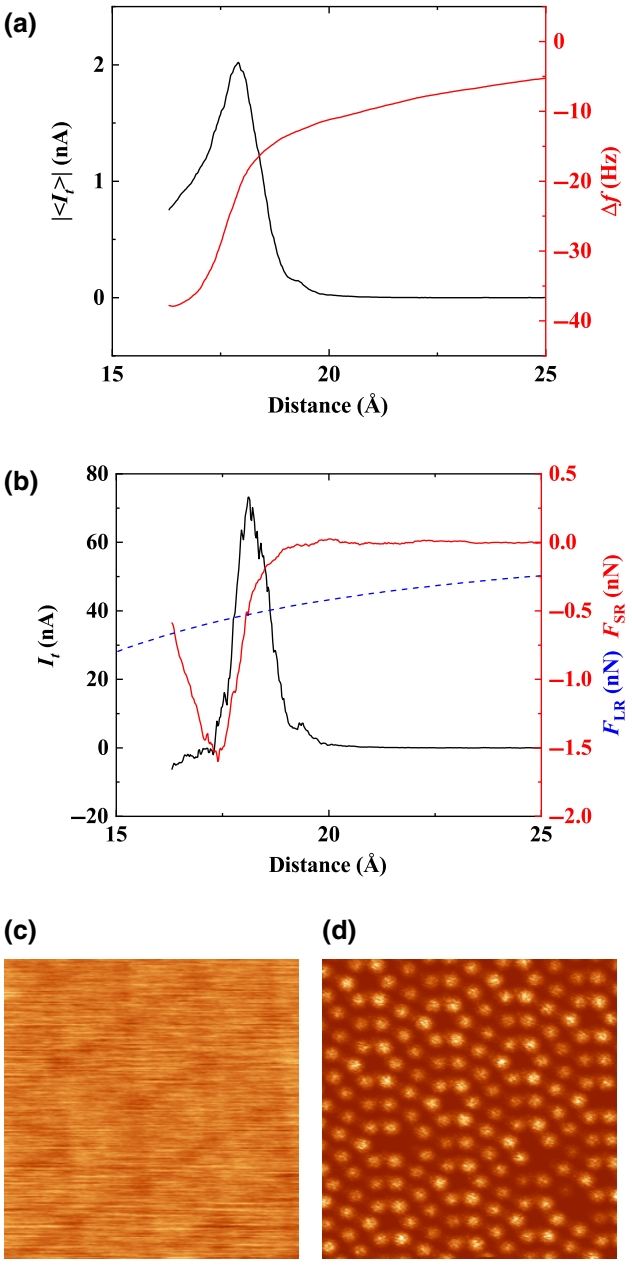

FIG. 5. Simultaneously obtained force and current spectroscopic data. (a) $\Delta f\,(z)$ (red) and $\langle I_t(z)\rangle$ (black) curves measured on the Si adatom in Fig. 4(a). (b) $F(z)$ and $I_t(z)$ (black) curves converted from the $\Delta f\,(z)$ and $\langle I_t(z)\rangle$ curves in (a). The $F(z)$ curve is deconvoluted to a short-range-force ($F_{\rm SR}$) curve (solid red line) and a long-range-force ($F_{\rm LR}$) curve (dotted blue line). AFM (c) and STM (d) images are simultaneously obtained with the AFM topographic mode [the set point of $\Delta f = -14.7$ Hz is represented by the blue arrow on the red curve in Fig. 4(a)]. The acquisition parameters as the same as for Fig. 4.

of the chemical bond [29,30]. The signatures of the current drop justify the existence of the Si cluster at the tip apex, from which the dangling bond of a Si atom protrudes toward the surface. Moreover, while the AFM image at a relatively long distance [the set point is indicated by the blue arrow on the red curve in Fig. 4(a)] does not show surface Si adatoms [Figs. 5(c)], the simultaneously observed STM image clearly shows the individual Si adatoms [Fig. 5(d)]. This contrast for the long-distance regime was reported previously [10], and is derived from the differences in the signal-to-noise ratio between AFM and STM.

IV. CONCLUSIONS

We investigate the *in situ* reproducibility of sharp Ag_2S tips for AFM. Ag_2S tips fabricated on conventional Si cantilevers show reversible growth and shrinkage of the Ag nanoprotrusion, controlled by the polarity of the bias voltage applied between the tip and the sample. Although the estimated radius of curvature of the Ag_2S base is much larger than that of normal Si and metal-coated Si tips, we are able to reduce the contribution of the long-range forces by fabricating a Ag nanoprotrusion on the Ag_2S base. Using the sharpened tip, we not only obtain atomic-resolution AFM images but also find that simultaneous AFM and STM measurements are possible. We expect the reproducible Ag nanoprotrusion on the Ag_2S base will be useful for scanning-tunneling luminescence spectroscopy [31,32] or tip-enhanced Raman spectroscopy [33] at the atomic scale. Thus, the *in situ* sharpening method achieved with Ag_2S tips has the potential to be widely used in the field of scanning-probe microscopy. The data that support the findings of this study are available from the corresponding author on reasonable request.

ACKNOWLEDGMENTS

We acknowledge support by Grants No. JP18H03859, No. 18K18990, No. 20H05178, and No. 20H05849. Y.S. acknowledges the support of the Asahi Glass Foundation and Toray Science Foundation.

APPENDIX: ESTIMATION OF THE HAMAKER CONSTANT

The nonretarded Hamaker constants between two half-spaces of material 1 and material 2 interacting across medium 3 can be calculated from the Lifshitz theory [34]:

$$A_{132} = \frac{3k_BT}{2}\sum_{m=0}^{\infty}{}'\sum_{s=0}^{\infty}\frac{(\Delta_{13}\Delta_{23})^s}{s^3}, \tag{A1}$$

where k_B and T are the Boltzmann constant and temperature, respectively, and

$$\Delta_{kl} = \frac{\varepsilon_k(i\xi_m) - \varepsilon_l(i\xi_m)}{\varepsilon_k(i\xi_m) + \varepsilon_l(i\xi_m)}, \tag{A2}$$

where $\varepsilon_k(i\xi_m)$ and $\varepsilon_l(i\xi_m)$ are the dielectric response function of material k and material l, respectively, of the

imaginary frequency $i\xi_m$. The frequency ξ_m (in radians per second) is sampled with a temperature-dependent interval (Matsubara frequency)

$$\xi_m = m\frac{4\pi^2 k_B T}{h}, \tag{A3}$$

where h is Planck's constant and m is a positive integer. The prime in the first summation in Eq. (A1) indicates that the static term ($m = 0$) should be given half weight. To evaluate the function $\varepsilon_k(i\xi_m)$, we need to know the dielectric response of the material k over the entire frequency range. With limited dielectric data available, the function $\varepsilon_k(i\xi_m)$ is usually represented by means of the Ninham-Parsegian approximation [35–38]. For simplicity, Hough and White [39] approximated $\varepsilon_k(i\xi_m)$ in the form

$$\varepsilon_k(i\xi_m) = 1 + \frac{C_{k,\mathrm{IR}}}{1 + (\xi_m/\omega_{k,\mathrm{IR}})^2} + \frac{C_{k,\mathrm{UV}}}{1 + (\xi_m/\omega_{k,\mathrm{UV}})^2}, \tag{A4}$$

where C_k and ω_k are the absorption strength and the relaxation frequencies in the IR and UV (or visible) ranges for material k, respectively. Hough and White showed that $\omega_{k,\mathrm{UV}}$ and $C_{k,\mathrm{UV}}$ can be obtained from the refractive index as a function of frequency, $n_k(\omega)$, in the visible and UV ranges by using the so-called Cauchy equation:

$$n_k^2(\omega) - 1 = [n_k{}^2(\omega) - 1]\frac{\omega^2}{\omega_{k,\mathrm{UV}}{}^2} + C_{k,\mathrm{UV}}, \tag{A5}$$

where a plot of $n^2(\omega) - 1$ versus $[n^2(\omega) - 1]\omega^2$ will give values of $\omega_{k,\mathrm{UV}}$ and $C_{k,\mathrm{UV}}$. The frequency of the IR oscillator can be readily obtained from the position of the bands in the IR spectra of the materials. The IR oscillator strength $C_{k,\mathrm{IR}}$ can be calculated from the static dielectric constant $\varepsilon_k(0)$:

$$C_{k,\mathrm{IR}} = \varepsilon_k(0) - C_{k,\mathrm{UV}} - 1. \tag{A6}$$

This equation is based on the close connection between $\varepsilon_k(i\xi_m)$ and $\varepsilon_k(m)$ and the approximation

$$\varepsilon_k(\omega) = \varepsilon_k'(\omega) + i\varepsilon_k''(\omega) \approx \varepsilon_k'(\omega) = n_k{}^2(\omega), \tag{A7}$$

where $\varepsilon_k'(\omega)$ and $\varepsilon_k''(\omega)$ are real and imaginary parts of the dielectric response function, respectively. More-simplified approximations of the Hamaker constant have been derived by retaining only a single UV term to represent the dielectric response of each material [40]. When $\varepsilon_k(0)(\equiv \varepsilon_k) \approx n_k(0)^2(\equiv n_k{}^2)$, the IR term can be ignored. Then, Eq. (A1) becomes

$$A_{132} = \frac{3k_BT}{4}\frac{(\varepsilon_1 - \varepsilon_3)(\varepsilon_2 - \varepsilon_3)}{(\varepsilon_1 + \varepsilon_3)(\varepsilon_2 + \varepsilon_3)} + \frac{3h\omega_{k,\mathrm{UV}}}{16\pi\sqrt{2}}\frac{(n_1{}^2 - n_3{}^2)(n_2{}^2 - n_3{}^2)}{\sqrt{n_1{}^2 + n_3{}^2}\sqrt{n_1{}^2 + n_3{}^2}\left(\sqrt{n_1{}^2 + n_3{}^2} + \sqrt{n_2{}^2 + n_3{}^2}\right)}. \tag{A8}$$

For two identical media ($\varepsilon_1 = \varepsilon_2 \neq \varepsilon_3, n_1 = n_2 \neq n_3$), Eq. (A8) becomes

$$A_{131} = \frac{3k_BT}{4}\left(\frac{\varepsilon_1 - \varepsilon_3}{\varepsilon_1 + \varepsilon_3}\right)^2 + \frac{3h\omega_{k,\mathrm{UV}}}{32\pi\sqrt{2}}\frac{(n_1{}^2 - n_3{}^2)^2}{(n_1{}^2 + n_3{}^2)^{3/2}}. \tag{A9}$$

Optical data for polycrystalline bulk Ag_2S were recently obtained by spectroscopic ellipsometry from 0.5 to 8.5 eV at room temperature [41]. The spectral parameters of the UV relaxation (adsorption strength $C_{k,\mathrm{UV}}$ and frequency $\omega_{k,\mathrm{UV}}$) are determined by our fitting the ellipsometry data to the Cauchy equation as shown in Fig. 6. The data are selected from the frequency range where the material displays a negligible extinction coefficient (below the band gap of 1.07 eV) and sufficiently above the IR absorption range [41]. The best-fitting line gives $\omega_{\mathrm{Ag_2S,UV}} = 4.7 \times 10^{15}$ rad/s and $C_{\mathrm{Ag_2S,UV}} = 7.9$. The static dielectric constant and refractive index of Ag_2S are taken from

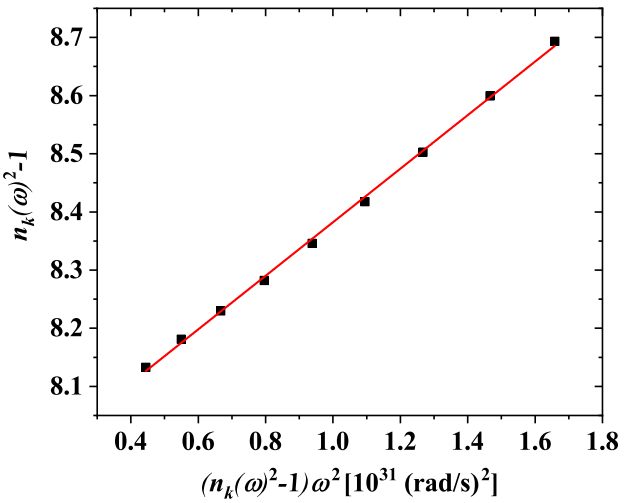

FIG. 6. Cauchy plot for Ag_2S. The red line represents the best-fitting line.

a database [42]: $\varepsilon_{Ag_2S} = 9.68$ and $n_{Ag_2S} = 2.69$, respectively. We assume a vacuum as medium 3, where $\varepsilon_{vac} = 1$ and $n_{vac} = 1$, respectively. By substituting these values and $T = 300$ K into Eq. (A9), we obtain

$$A_{Ag_2S\text{-vac-}Ag_2S} = 1.1 \times 10^{-19}\ \text{J}. \tag{A10}$$

To calculate the Hamaker constant for the mixed system of Ag_2S, a vacuum, and Si, we apply the geometric mean [43] to $A_{Ag_2S\text{-vac-}Ag_2S}$ and $A_{Si\text{-vac-}Si} = 1.865 \times 10^{-19}$ J [3], and finally obtain

$$A_{Ag_2S\text{-vac-}Si} = \sqrt{A_{Ag_2S\text{-vac-}Ag_2S} \times A_{Si\text{-vac-}Si}} = 1.4 \times 10^{-19}\ \text{J}. \tag{A11}$$

[1] F. J. Giessibl, Atomic resolution of the silicon (111)-(7 × 7) surface by atomic force microscopy, Science **267**, 68 (1995).

[2] L. Gross, F. Mohn, N. Moll, P. Liljeroth, and G. Meyer, The chemical structure of a molecule resolved by atomic force microscopy, Science **325**, 1110 (2009).

[3] M. A. Lantz, H. J. Hug, R. Hoffmann, P. J. A. van Schendel, P. Kappenberger, S. Martin, A. Baratoff, and H.-J. Güntherodt, Quantitative measurement of short-range chemical bonding forces, Science **291**, 2580 (2001).

[4] Y. Sugimoto, P. Pou, M. Abe, P. Jelínek, R. Pérez, S. Morita, and O. Custance, Chemical identification of individual surface atoms by atomic force microscopy, Nature **446**, 64 (2007).

[5] J. Onoda, H. Miyazaki, and Y. Sugimoto, Chemical identification of the foremost tip atom in atomic force microscopy, Nano Lett. **20**, 2000 (2020).

[6] J. Onoda, M. Ondráček, P. Jelínek, and Y. Sugimoto, Electronegativity determination of individual surface atoms by atomic force microscopy, Nat. Commun. **8**, 15155 (2017).

[7] F. J. Giessibl, Advances in atomic force microscopy, Rev. Mod. Phys. **75**, 949 (2003).

[8] F. J. Giessibl, Atomic resolution on si (111)-(7 × 7) by noncontact atomic force microscopy with a force sensor based on a quartz tuning fork, Appl. Phys. Lett. **76**, 1470 (2000).

[9] Y. Sugimoto and J. Onoda, Force spectroscopy using a quartz length-extension resonator, Appl. Phys. Lett. **115**, 173104 (2019).

[10] Y. Sugimoto, Y. Nakajima, D. Sawada, K.-I. Morita, M. Abe, and S. Morita, Simultaneous afm and stm measurements on the si (111)-(7 × 7) surface, Phys. Rev. B **81**, 245322 (2010).

[11] H. Dai, J. H. Hafner, A. G. Rinzler, D. T. Colbert, and R. E. Smalley, Nanotubes as nanoprobes in scanning probe microscopy, Nature **384**, 147 (1996).

[12] T. Ikuno, M. Katayama, M. Kishida, K. Kamada, Y. Murata, T. Yasuda, S.-I. Honda, J.-G. Lee, H. Mori, and K. Oura, Metal-coated carbon nanotube tip for scanning tunneling microscope, Jpn. J. Appl. Phys. **43**, L644 (2004).

[13] J. Martínez, T. Yuzvinsky, A. Fennimore, A. Zettl, R. García, and C. Bustamante, Length control and sharpening of atomic force microscope carbon nanotube tips assisted by an electron beam, Nanotechnology **16**, 2493 (2005).

[14] G. Phillips, M. Siekman, L. Abelmann, and J. Lodder, High resolution magnetic force microscopy using focused ion beam modified tips, Appl. Phys. Lett. **81**, 865 (2002).

[15] H. Labidi, M. Kupsta, T. Huff, M. Salomons, D. Vick, M. Taucer, J. Pitters, and R. A. Wolkow, New fabrication technique for highly sensitive qplus sensor with well-defined spring constant, Ultramicroscopy **158**, 33 (2015).

[16] M. Rezeq, J. Pitters, and R. Wolkow, Tungsten nanotip fabrication by spatially controlled field-assisted reaction with nitrogen, J. Chem. Phys. **124**, 204716 (2006).

[17] F. Rahman, J. Onoda, K. Imaizumi, and S. Mizuno, Field-assisted oxygen etching for sharp field-emission tip, Surf. Sci. **602**, 2128 (2008).

[18] J. Onoda, S. Mizuno, and H. Ago, Stem observation of tungsten tips sharpened by field-assisted oxygen etching, Surf. Sci. **604**, 1094 (2010).

[19] J. Falter, G. Langewisch, H. Hölscher, H. Fuchs, and A. Schirmeisen, Field ion microscopy characterized tips in noncontact atomic force microscopy: Quantification of long-range force interactions, Phys. Rev. B **87**, 115412 (2013).

[20] F. Mohn, B. Schuler, L. Gross, and G. Meyer, Different tips for high-resolution atomic force microscopy and scanning tunneling microscopy of single molecules, Appl. Phys. Lett. **102**, 073109 (2013).

[21] A. Shiotari, T. Odani, and Y. Sugimoto, Torque-Induced Change in Configuration of a Single no Molecule on Cu (110), Phys. Rev. Lett. **121**, 116101 (2018).

[22] K. Terabe, T. Nakayama, T. Hasegawa, and M. Aono, Formation and disappearance of a nanoscale silver cluster realized by solid electrochemical reaction, J. Appl. Phys. **91**, 10110 (2002).

[23] K. Terabe, T. Hasegawa, T. Nakayama, and M. Aono, Quantized conductance atomic switch, Nature **433**, 47 (2005).

[24] T. Hino, T. Hasegawa, K. Terabe, T. Tsuruoka, A. Nayak, T. Ohno, and M. Aono, Atomic switches: Atomic-movement-controlled nanodevices for new types of computing, Sci. Technol. Adv. Mater. **12**, 013003 (2011).

[25] M. Abe, Y. Sugimoto, O. Custance, and S. Morita, Room-temperature reproducible spatial force spectroscopy using atom-tracking technique, Appl. Phys. Lett. **87**, 173503 (2005).

[26] J. E. Sader and S. P. Jarvis, Accurate formulas for interaction force and energy in frequency modulation force spectroscopy, Appl. Phys. Lett. **84**, 1801 (2004).

[27] Y. Sugimoto, A. Yurtsever, M. Abe, S. Morita, M. Ondráček, P. Pou, R. Pérez, and P. Jelínek, Role of tip chemical reactivity on atom manipulation process in dynamic force microscopy, ACS Nano. **7**, 7370 (2013).

[28] J. E. Sader and Y. Sugimoto, Accurate formula for conversion of tunneling current in dynamic atomic force spectroscopy, Appl. Phys. Lett. **97**, 043502 (2010).

[29] P. Jelínek, M. Švec, P. Pou, R. Perez, and V. Cháb, Tip-Induced Reduction of the Resonant Tunneling Current on Semiconductor Surfaces, Phys. Rev. Lett. **101**, 176101 (2008).

[30] D. Sawada, Y. Sugimoto, K.-i. Morita, M. Abe, and S. Morita, Simultaneous measurement of force and tunneling

current at room temperature, Appl. Phys. Lett. **94**, 173117 (2009).

[31] H. Imada, K. Miwa, M. Imai-Imada, S. Kawahara, K. Kimura, and Y. Kim, Real-space investigation of energy transfer in heterogeneous molecular dimers, Nature **538**, 364 (2016).

[32] K. Kimura, K. Miwa, H. Imada, M. Imai-Imada, S. Kawahara, J. Takeya, M. Kawai, M. Galperin, and Y. Kim, Selective triplet exciton formation in a single molecule, Nature **570**, 210 (2019).

[33] R. Zhang, Y. Zhang, Z. Dong, S. Jiang, C. Zhang, L. Chen, L. Zhang, Y. Liao, J. Aizpurua, Y. e. Luo, and *et al.*, Chemical mapping of a single molecule by plasmon-enhanced raman scattering, Nature **498**, 82 (2013).

[34] L. Bergström, Hamaker constants of inorganic materials, Adv. Colloid Interface Sci. **70**, 125 (1997).

[35] V. Parsegian and B. Ninham, Application of the lifshitz theory to the calculation of van der waals forces across thin lipid films, Nature **224**, 1197 (1969).

[36] B. Ninham and V. Parsegian, Van der waals forces: Special characteristics in lipid-water systems and a general method of calculation based on the lifshitz theory, Biophys. J. **10**, 646 (1970).

[37] J. Mahanty and B. W. Ninham, *Dispersion Forces* (Academic Press, London, 1976), Vol. 1.

[38] D. C. Prieve and W. B. Russel, Simplified predictions of hamaker constants from lifshitz theory, J. Colloid Interface Sci. **125**, 1 (1988).

[39] D. B. Hough and L. R. White, The calculation of hamaker constants from liftshitz theory with applications to wetting phenomena, Adv. Colloid Interface Sci. **14**, 3 (1980).

[40] D. Tabor and R. Winterton, The direct measurement of normal and retarded van der waals forces, Proc. R. Soc. London, A **312**, 435 (1969).

[41] M. Diware, S. Ganorkar, J. Kim, S. Bramhe, H. Cho, Y. Cho, and W. Chegal, Dielectric function of polycrystalline α-Ag_2S by spectroscopic ellipsometry, Appl. Phys. Lett. **107**, 171905 (2015).

[42] A. Jain, S. P. Ong, G. Hautier, W. Chen, W. D. Richards, S. Dacek, S. Cholia, D. Gunter, D. Skinner, G. Ceder, and K. a. Persson, The materials project: A materials genome approach to accelerating materials innovation, APL Mater. **1**, 011002 (2013).

[43] N. F. Owens and P. Richmond, Hamaker constants and combining rules, J. Chem. Soc., Faraday Trans. 2 **74**, 691 (1978).